Geochemical Perspectives Letters

Reliability of Raman analyses of CO_2-rich fluid inclusions as a geobarometer at Kīlauea

C.L. DeVitre, P.E. Wieser

Supplementary Information

The Supplementary Information includes:

- 1. Detailed Materials and Methods
- 2. Statistical Significance of the MI *vs*. FI Recorded Pressures
- 3. Fluid % Effect on Calculated Densities and Pressures
- Figures S-1 to S-13
- Tables S-1 to S-7
- Supplementary Image Database
- Supplementary Information References

All raw data, including spectra, fitting images and Jupyter Lab notebooks to process and plot data can be found on the Github repository https://github.com/cljdevitre/KilaueaMIFI2023, which is archived on Zenodo (https://zenodo.org/doi/10.5281/zenodo.10520936).

1. Detailed Materials and Methods

1.1 Samples

Olivines from three samples of the 2018 LERZ eruption of Kīlauea volcano in Hawai'i (Fissure 8 samples of May, July and August 2018) were picked under a binocular microscope, and individually mounted in CrystalBond™ on glass slides from jaw crushed and sieved samples as described in Wieser *et al.* (2021). The May 2018 sample erupted on 30 May 2018 (Lab code LL4, USGS code KE62–3293), as vesicular reticulite and scoria; The July 2018 sample erupted in mid-July, 2018 (Lab code LL8, no USGS code) was sampled from the selvages of a naturally quenched, and highly vesicular proximal overflow from the Fissure 8 channel; The August 2018 sample erupted on 1 August 2018 (Lab code LL7, USGS code KE62–A3321F) and was sampled directly from the channel and rapidly quenched in water (Wieser *et al.*, 2021). FI were revealed by grinding using 250–3000 grade wet and dry paper. Petrographic work was done to describe the emplacement of FI and FIA in the crystals. Photos were taken of the crystals and FI (see SI Image Database). Additionally, FI were located and photographed in the same crystals as those in which melt inclusions were analysed in Wieser *et al.* (2021). In total we analysed 145 FI hosted in 57 olivine crystals from the 2018 LERZ eruption of Kīlauea volcano. In the final dataset (102 fluid inclusions), we discarded spectra that yielded density errors

>20 % due to poor spectral quality (*e.g.*, high and/or wavy backgrounds, low signal/noise ratio) and excluded fluid inclusions with a melt film that occupied more than 20 % of the inclusion volume.

Olivines from tephra of the 1951 eruption of Fogo Volcano in Cabo Verde (DeVitre *et al.*, 2023), were also picked under binocular microscope and individually mounted in CrystalBond™. FI were revealed by grinding using 600–2000 grit wet paper and polish refined using 1 and 0.3 µm wet paper and alumina paste. These crystals were doubly polished for micro thermometric analyses. We analysed 63 FI in 12 crystals of this eruption *via* Raman and microthermometry.

1.2 Raman Spectroscopy FI CO_2

We collected Raman spectra using a WiTec Alpha 300R Raman spectrometer at the Department of Earth and Planetary Sciences at the University of California, Berkeley. We use a green solid state 532.046 nm laser focused as an excitation source with a 50x objective (x0.55NA, 9.1 mm focal distance) and 100x objective (x0.95NA, 4 mm WD). The system is equipped with TruePower system which allows for in-fiber power adjustments of <0.1 mW. We used a power of 6–12 mW. We used an FDCA built following the method of DeVitre *et al.* (2021)with an extended upper pressure limit from 35 to up to 68 MPa (through use of a sapphire window instead of fused silica-quartz) to produce calibration equations relating CO_2 density and Δ_{CO_2} for our instrument. These equations are available in DiadFit (Wieser and DeVitre, 2023) and have the same functional form as those reported in DeVitre *et al.* (2021) with updated coefficients.

Spectra for FI were collected at 37 °C, with temperature regulated at 37 °C using a Peltier thermoelectric stage with a centre hole fixed on a magnetic aluminum holder. Spectra were acquired with five accumulations of 45 s of integration time (total analytical time = 225 s) in a single window using 1800 grooves/mm (~0.54 cm^{-1} spectral resolution) and a spectral centre of 1325 cm^{-1}. We discarded spectra with less than three points above the background (these yield spurious fits with up to >100 % error on fitting), those with high backgrounds interfering with the fit and those with normalised Intensity/FWHM < 200 according to the criteria of Yuan and Mayanovic (2017) as these cannot be fit confidently. A filtered total of 124 FI yielded results with 1σ in CO_2 density better than ~0.02 g/mL (Table S-1).

Neon (Ne) spectra were collected every ~10–15 minutes using the same grating and spectral centre as the unknown and three accumulations of 45 s integration time, to correct for non-linearity of the Raman shift axis (Lin *et al.*, 2007; Wang *et al.*, 2011; Lamadrid *et al.*, 2017; DeVitre *et al.*, 2021).

All spectra were processed using the Python tool DiadFit v0.0.62 (Wieser and DeVitre, 2023). Spectra are baseline-subtracted prior to fitting (2nd degree polynomial baseline subtraction anchored on either side of peak of interest), and we fit a Pseudo-Voigt peak (mixed Gaussian and Lorentzian model) on each main CO_2 peak (1285 cm^{-1} and 1389 cm^{-1}). Voigt and Pseudo-Voigt functional forms are typically considered the most appropriate for symmetric Raman peaks (*e.g.*, single-phase CO_2 peaks and Neon emission lines; Yuan and Mayanovic, 2017). For fitting, CO_2 spectra were separated into three groups based on overall intensity of the spectra, and overlap between main peaks, hot bands (1270 cm^{-1} and 1410 cm^{-1}) and ^{13}C (1370 cm^{-1}) such that additional peaks were simultaneously fit when needed to reduce the effect of residuals on the fit (Jupyter notebooks are included in the supplement). We corrected our data following the methods of Lamadrid *et al.* (2017) and DeVitre *et al.* (2021) using two known Ne emission lines (1117.086987 cm^{-1} and 1447.564622 cm^{-1}) that encompass the Fermi diad. A single Voigt peak is fit at 1446–1453 cm^{-1} for the upper line while two Voigt peaks (1113–1120 cm^{-1} and 1115–1122 cm^{-1}) are used for the lower line since it appears as a double-peak at out spectral resolution. We calculated the instrumental drift correction factor Ne_{coeff} as:

$$Ne_{coeff} = \left(\frac{\Delta Ne_{known}}{\Delta Ne_{observed}}\right) \quad \text{(S-1)}$$

where ΔNe_{known} is the theoretical separation of the Ne emission lines in air and $\Delta Ne_{observed}$ is the measured separation of the same Ne emission lines on the Raman spectrum.

We then modelled the instrumental drift during each session as a polynomial function (typically 1st to 3rd degree polynomial, unless large temperature fluctuations happened during the session) relating Ne_{coeff} to time in seconds. Exact timestamps are extracted for each CO_2 spectrum and the appropriate Ne_{coeff} from the model is applied to correct the separation of the Fermi Diad. We also fit and calculated areas for SO_2 and CO_3 when observed on the spectra; these were fit as gaussian functions.

We calculated densities using the appropriate calibrated density equations for our instrument using DiadFit (Wieser and DeVitre, 2023). We estimated entrapment temperatures from the Fo content of the olivine (see below). We then calculated pressures from measured densities and estimated entrapment temperatures using the EOS of Span and Wagner (1996) and propagated uncertainty using Monte Carlo simulations. Finally, we calculated the depths of entrapment using the crustal density model of Ryan (1987), described in Lerner *et al.* (2021) for Hawai‘i.

1.3 Quantifying Uncertainty and Reproducibility of Measurements of Fluid Inclusions

Uncertainties on fluid inclusion pressures were propagated in DiadFit, using Monte Carlo simulations considering 50 K uncertainty on the Temperature (see section 1.5) and 1σ uncertainty on density from peak-fit uncertainties on CO_2 spectra and the uncertainty in the Ne correction model estimated by DiadFit. The majority of data presented in the paper was fitted with DiadFit version v0.0.62. This version propagates the uncertainty in peak position into calculated densities. A newer version of DiadFit (v0.0.78) that was released recently also accounts for the error from the densimeter and drift correction model. To assess differences between these errors, we refit a subset of Raman data (17 October 2022; see Table S-3 and data repository) that encompasses most CO_2 densities found in our study (Wieser and DeVitre, 2023). We did not apply filters for bad spectra (*e.g.*, high background, too little intensity/number of points to fit) for this exercise. It is immediately apparent that the error for our measurements predominantly arises from the error involved in fitting Diad peaks (Fig. S-1), and that the error on the densimeter and Ne line correction plays only a minor role in most cases (Fig. S-1c, d; <10 %). Additionally, the densities and associated errors calculated by version v0.0.62 are not significantly different from those calculated by v0.0.78 (Fig. S-2), and both lie on a 1:1 line. The densities calculated densities with v.0.078 are within 0.004 g/cm^3 of those calculated with v.0.062 and except for four data points, the majority are within 0.001 g/cm^3. The calculated errors are for the most part within 0.002 g/cm^3 except for two points (one at 0.004 g/cm^3 and one at 0.01 g/cm^3). We note that these two datapoints as well as some others were discarded in the final dataset due to low intensity and/or high backgrounds which largely accounts for the high fitting error. Overall, this shows that for the samples examined in this study, the peak fitting errors from v0.0.62 are a reasonable estimate, and complete refitting of the dataset is not justified.

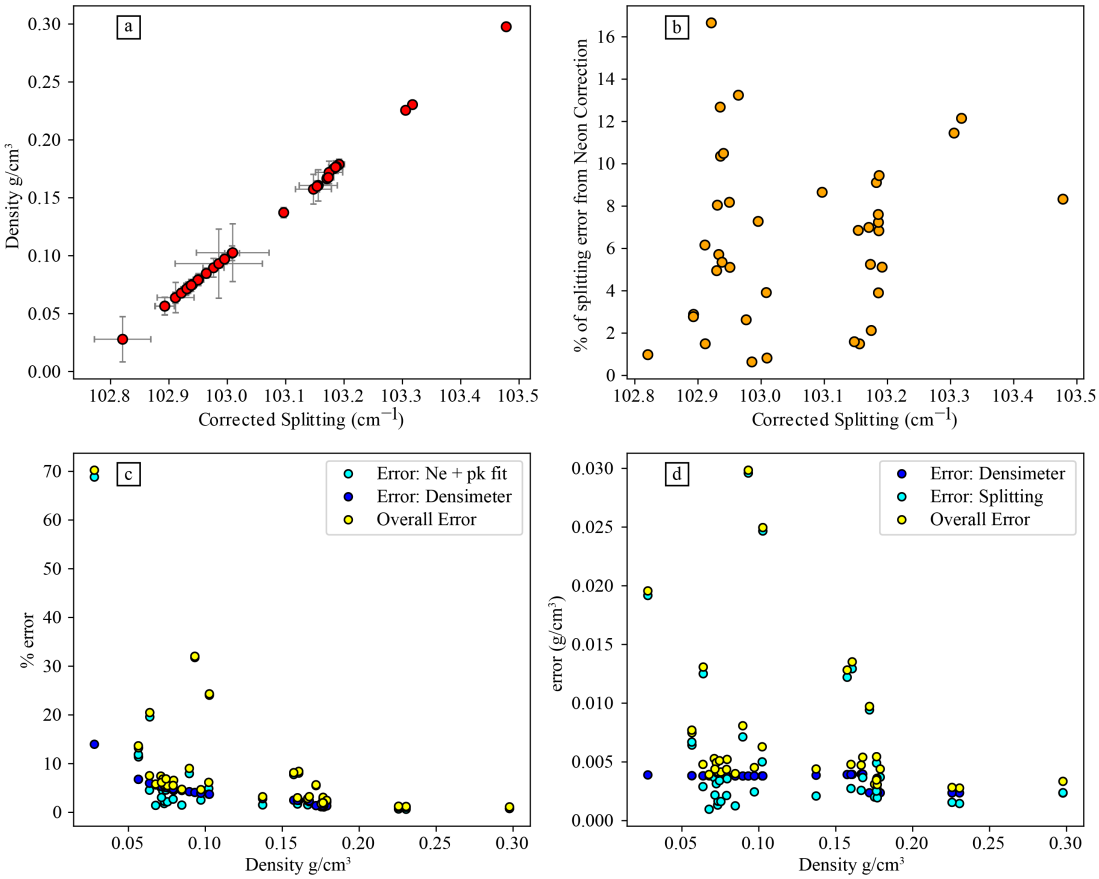

Figure S-1 Refit Raman data from 17 October 2022 using DiadFit v0.0.78. **(a)** Separation of the Fermi Diad *vs.* CO_2 density with error bars shown in black. **(b)** Percentage of the error on the Fermi Diad separation that is due to the Neon Correction. **(c)** Percentage of error in CO_2 density *vs*. CO_2 density. Yellow dots are the overall error (from all sources), cyan dots are the error from peak fitting and neon correction alone and blue dots are the error from the densimeter only. **(d)** Absolute error in CO_2 density *vs*. CO_2 density. Yellow dots are the overall error (from all sources), cyan dots are the error from peak fitting and neon correction alone and blue dots are the error from the densimeter only.

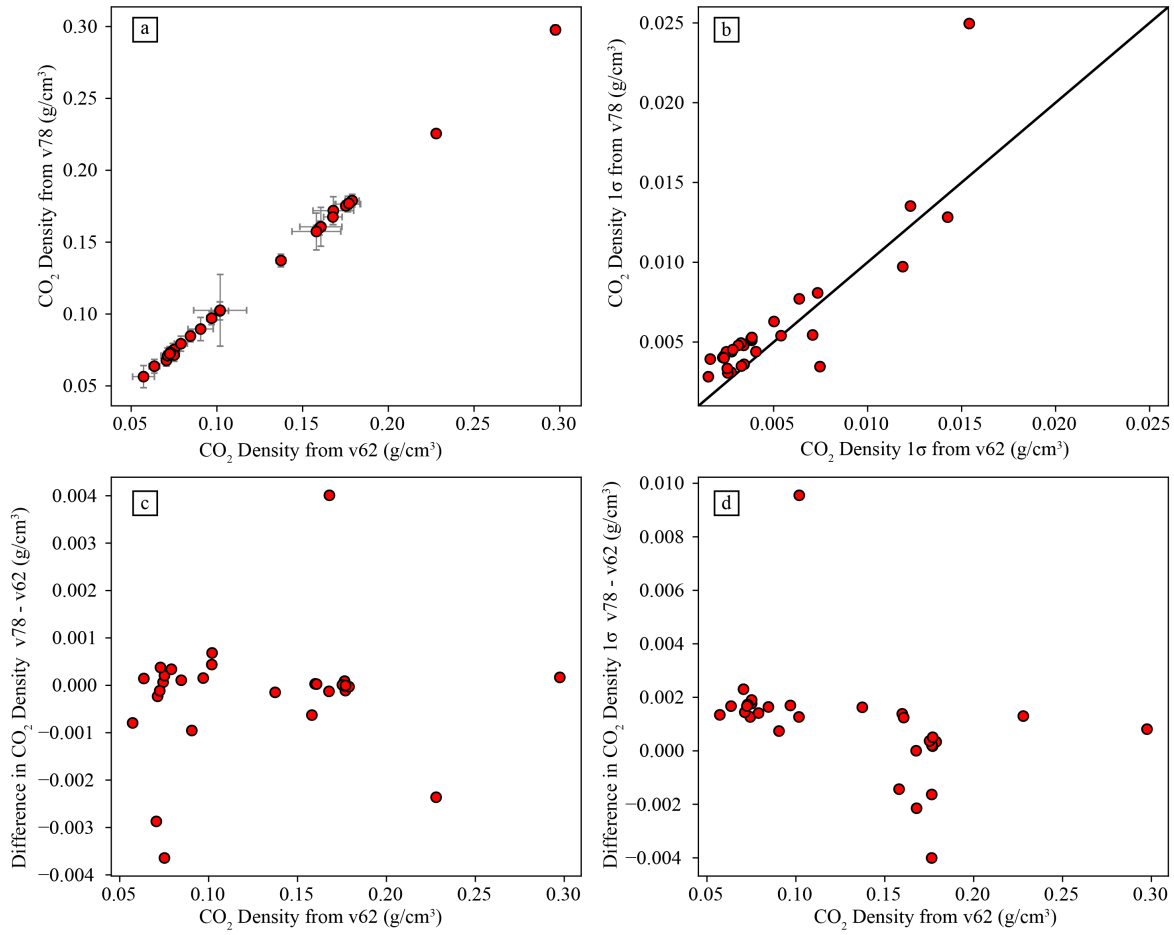

Figure S-2 Refit Raman data from 17 October 2022 using DiadFit v0.0.78 *vs*. original data fit using DiadFit v0.0.62. **(a)** CO_2 density from version v0.0.78 *vs.* from version v0.0.62 with error bars shown in black. **(b)** CO_2 density 1σ error from version v0.0.78 *vs*. from version v0.0.62. **(c)** Difference in CO_2 density from v78 and CO_2 density from v62. **(d)** Difference in CO_2 density 1σ error from v78 and CO_2 density 1σ from v62.

We also assessed the reproducibility of our measurements based on repeated analyses of single fluid inclusions (Fig. S-3). For repeated measurements, the standard deviation is no higher than 0.02 g/cm^3, even when the measurements were repeated on different days (Fig. S-3a, b). Further, the 1σ error output from DiadFit is similar to the standard deviation of repeated measurements and is often slightly higher. Overall, only one measurement in our reported dataset has a 1σ > 0.02 g/cm^3, which indicates that the use of a CO_2 density error of ~0.02 g/cm^3 in the Monte Carlo error simulations is appropriate to describe the error in our dataset. This also matches the findings of Dayton *et al.* (2023) based on their repeated measurements using identical instrument and calibration hardware.

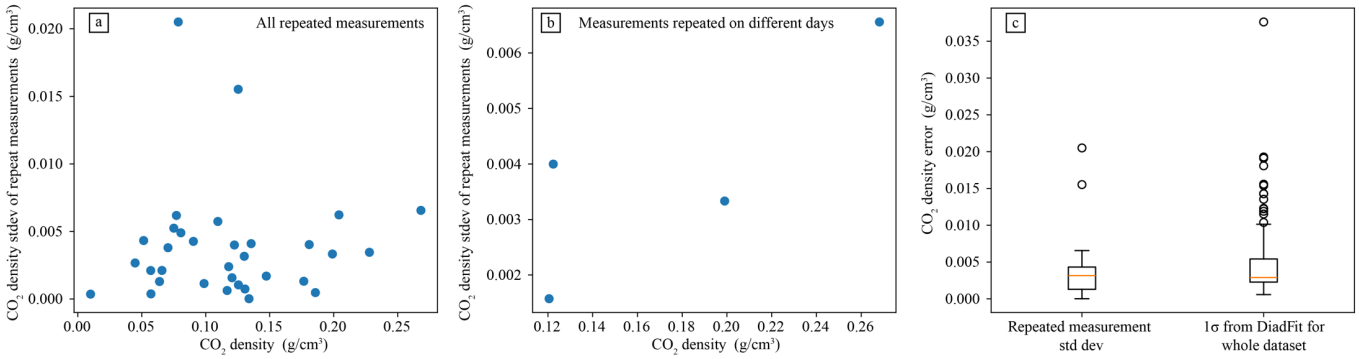

Figure S-3 Comparison of error from DiadFit and reproducibility of repeated measurements. **(a)** Standard deviation of repeated measurements *vs*. CO_2 density. This plot includes measurements that were repeated on the same day (consecutive repeated measurements) as well as those that were repeated on a different day. **(b)** Standard deviation of repeated measurements *vs*. CO_2 density considering only measurements with repeats on different days (for the same fluid inclusion at least one of the repeats was on a different day). **(c)** Box plots of CO_2 density error for two groups: repeated measurements (this is the standard deviation of N repeated measurements) and the reported error calculated from DiadFit. This demonstrates the error estimated by DiadFit is a good match to the error determined by repeated measurements.

1.4 Microthermometry of FI

For samples with bulk CO_2 densities above the critical density of CO_2 (~0.45 g/mL), we conducted microthermometry experiments to obtain the freezing and homogenisation temperatures and calculate an independent estimate of the CO_2 density of the FI. It was not possible to obtain microthermometric data for FI that homogenise to vapor, as it is difficult to observe the homogenisation of the thin liquid film into vapor in our samples. These experiments were conducted using a Linkam THMSG600 heating and freezing stage, with environmental control from −195 °C to +600 °C, equipped with a liquid nitrogen cooling pump allowing for cooling rates from 0.01 to 150 °C/min. We used a CO_2–H_2O standard to calibrate the melting temperature of CO_2 (−56.6 °C) and a pure H_2O standard to calibrate the melting temperature (0.0 °C). All experiments were done using the cycling technique (Hansteen and Klügel, 2008) to ensure that homogenisation was completed. We then converted the homogenisation temperatures to CO_2 density using the EOS of Span and Wagner (1996) implemented in DiadFit (Wieser and DeVitre, 2023). All FI were found to have melting temperatures of −56.5 ± 0.1 °C (Fig. S-4a), indicating that they are pure CO_2.

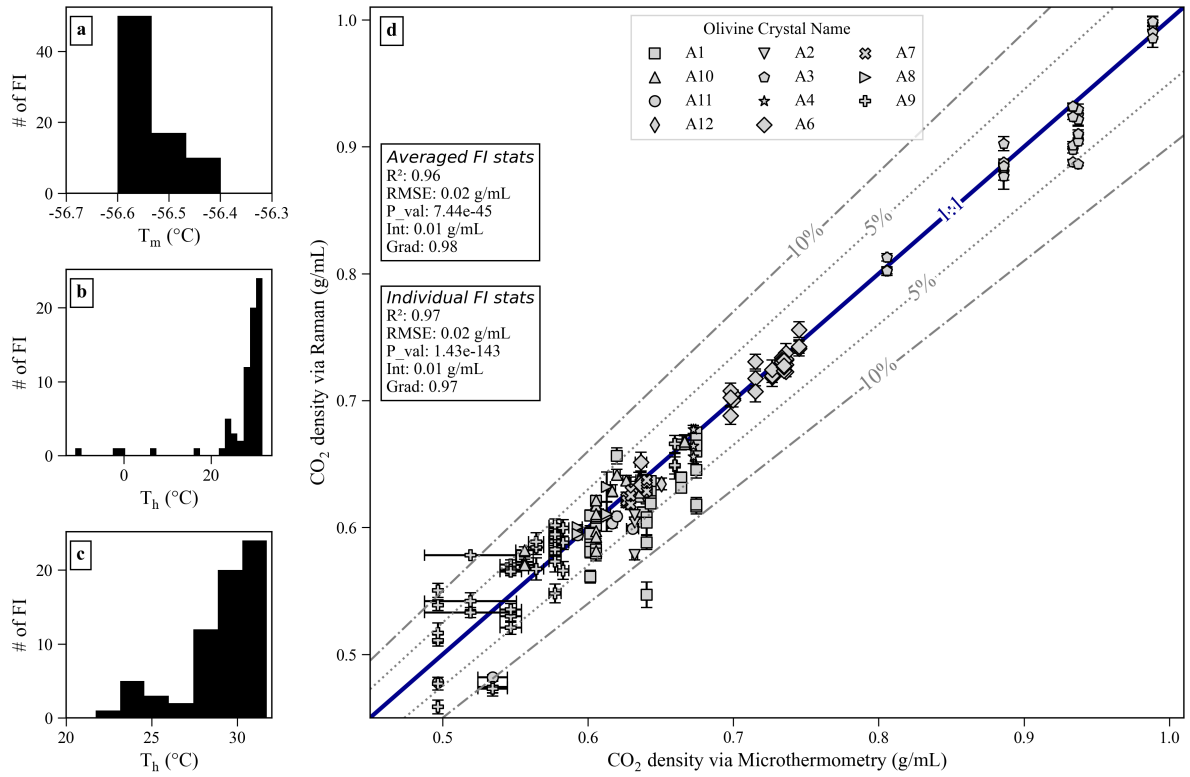

Figure S-4 CO_2 densities *via* microthermometry *versus* calibrated Raman Spectroscopy. **(a)** Freezing temperatures of FI. **(b)** Homogenisation temperatures of FI (all FI homogenised to liquid). **(c)** Close-up of panel **(b)**. **(d)** Density *via* Raman *vs*. density *via* micro thermometry. FIs in the same crystal are plotted with the same symbol. Error bars for Raman-based CO_2 densities are propagated fitting + Neon correction uncertainties while error bars for microthermometry are the standard deviation of homogenisation temperatures obtained during cycling.

Under Raman spectroscopy, none of the FI analysed had detectable amounts of any other gases, however they contained variable amounts of carbonate. Homogenisation temperatures ranged from −11.1 ± 0.2 °C to +31.6 ± 1 °C (Fig S-1b, c), measurements with homogenisation temperatures close to critical were more difficult to perform and the uncertainty on the temperature is therefore higher, limited by the high $\Delta\rho/\Delta T$ and the accuracy of the temperature controller of the stage. We only calculate and report CO_2 densities from microthermometry when the homogenisation temperature was determined with reasonable confidence. Peak-fitting and drift and precision account for most of the uncertainty for Raman (see Fig. 8 in Wieser and DeVitre, 2023), while the uncertainty for microthermometry can be attributed to difficulty in observing the phase homogenisation near and/or below the critical density of CO_2, thermocouple accuracy and precision of thermal control. For densities close to critical (~0.45 g/mL), the uncertainty on microthermometry measurements significantly increases due to much higher $\Delta\rho/\Delta T$—such that very small uncertainties in the homogenisation temperature can cause much larger uncertainties in the density (Hansteen and Klügel, 2008).

1.5 Host Olivine Chemistry

Spot analyses of host olivines were conducted using a JEOL JXA-8230 EPMA in the Mineral and Microchemical Analysis Facility at Stanford University. Counting statistics and other analytical conditions

along with repeated analyses of secondary standards (San Carlos Olivine, Stillwater olivine; Jarosewich *et al.*, 1980) are presented in Table S-5. We note that melt inclusion olivine hosts reported in Wieser *et al.* (2021) were analysed using the University of Cambridge's Cameca SX100 EPMA in the Department of Earth Sciences. For consistency in our comparisons, we correct the Fo contents (mol %) of our fluid inclusion olivine hosts obtained from the Stanford EPMA data to Fo contents that would have been obtained had they been analysed on the Cambridge EPMA instead. To do this, we analysed spots on a subset of olivines from Wieser *et al.* (2021) which had previously been analysed at Cambridge, based on detailed BSE maps. We then performed a linear regression of olivine host Fo contents from Stanford and Cambridge and use the equation to correct our fluid inclusion olivine host Fo content data. The equation is as follows: $\mathrm{Fo}_{\mathrm{Cambridge}} = 0.9815 \times \mathrm{Fo}_{\mathrm{Stanford}} + 0.893$.

Entrapment temperatures were estimated from the host olivine Fo content by developing an olivine-only thermometer suitable for Kīlauea. The Fo content of an olivine is a function of the MgO and FeO_T content of the liquid from which it equilibrates with, the Ol-Liq partition coefficient, and the proportion of Fe^{3+} in the liquid. Fortunately, Ol-saturated liquids at Kīlauea have a relatively constant FeO content (see Fig. S-5). Thus, if the Fo content is known, the K_D is known, the Fe^{3+} ratio is known, and the FeO_T content can be relatively constant, the Fo content can be related to MgO, which in turn, can be related to temperature at Kīlauea.

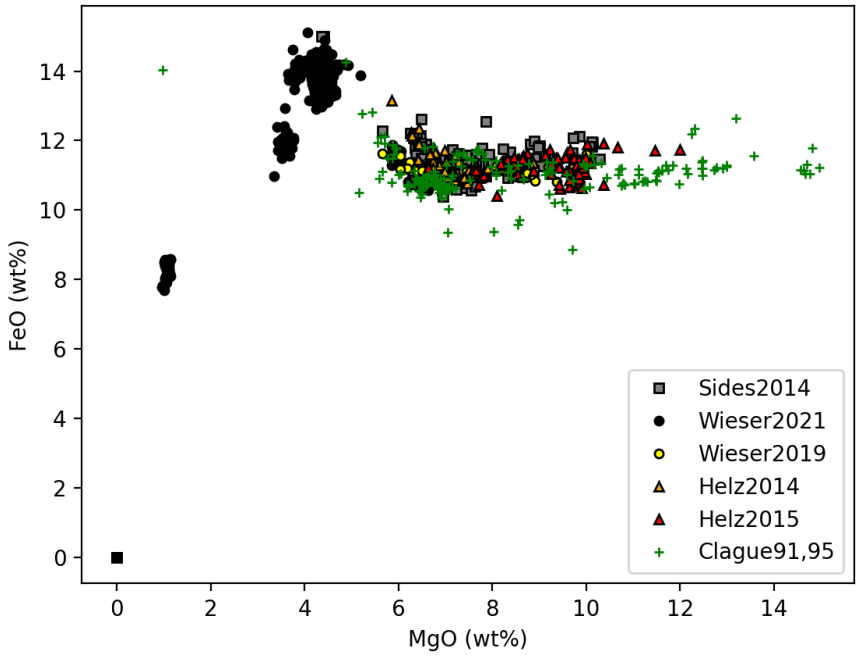

Figure S-5 Compiled glass data used to calibrate an Ol-only thermometer (Clague and Bohrson, 1991; Clague *et al.*, 1995; Helz *et al.*, 2014, 2015; Sides *et al.*, 2014a, 2014b; Wieser *et al.*, 2019, 2021).

To calibrate the Ol-only thermometer, we calculated a liquid-only temperature using the new MgO-thermometer of Shea *et al.* (2022) for each liquid in our compiled dataset. We also calculated an equilibrium olivine content using the K_D model of Shea *et al.* (2022), assuming $Fe^{3+}/Fe_T = 0.15$ (Moussallam *et al.*, 2016; Helz *et al.*, 2017; Lerner *et al.*, 2021). We then fit a 3rd degree polynomial between temperature and Ol Fo content (Fig. S-6). We also show the polynomial that would result from using $Fe^{3+}/Fe_T = 0.2$ instead. This is well within the ±50 K uncertainty used for temperature for the Monte-Carlo simulations (red dashed lines).

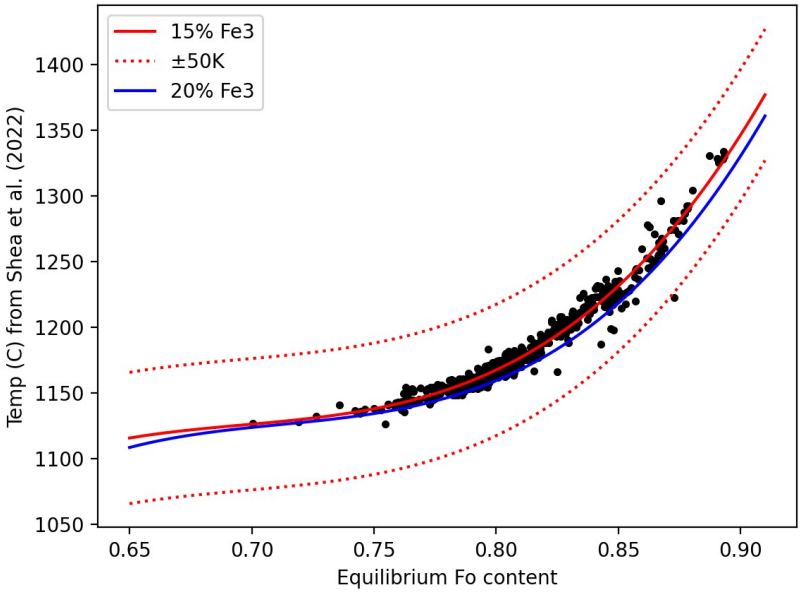

Figure S-6 3rd degree polynomial fit between equilibrium Fo content and temperature calculated from the glass composition using the thermometer of Shea *et al.* (2022).

We tested the success of this Ol-only thermometer on the experimental data used to calibrate the expressions of Shea *et al.* (2022). We note that these experimental liquids have far more diversity in FeO content than natural Kīlauea liquids, which explains the larger discrepancies that exist. If we restrict comparison to liquids within the mean ± 1σ of the observed distribution of Kīlauean liquids, we can see the method is successful within the ±50 K uncertainty allocated for Monte Carlo methods (pink box, Fig. S-7).

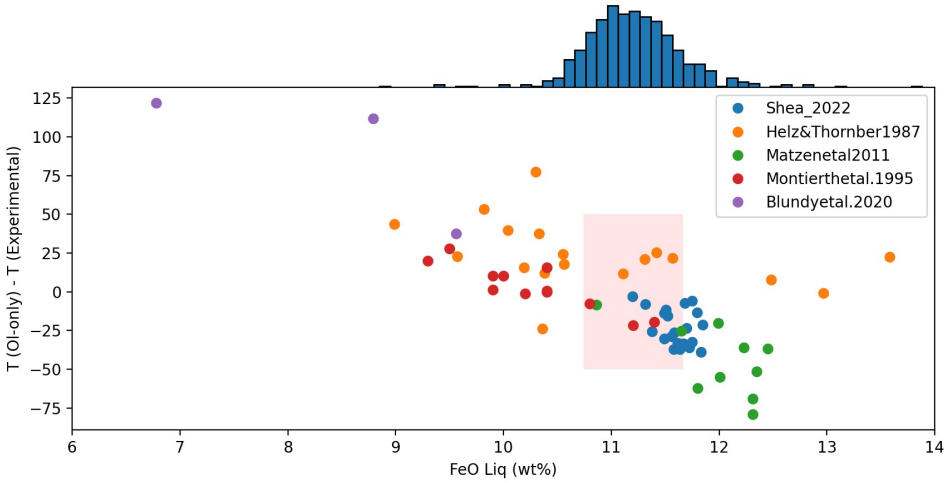

Figure S-7 Assessing the Ol-only thermometer on the calibration dataset of Shea *et al.* (2022). The distribution of FeO contents in natural Kīlauea liquids is shown with the blue histogram. In the pink shaded box, we highlight experimental liquids within the mean ± 1σ of this distribution. These experiments lie well within the 1σ = 50 K uncertainty allocated for entrapment temperatures. Data from Helz and Thornber (1987), Montierth *et al.* (1995), Matzen *et al.* (2011), Blundy *et al.*(2020), Shea *et al.* (2022).

1.6. Estimating SO_2/CO_2 Ratios in FI

To estimate the SO_2 fraction in our FI, we calculated the area under the SO_2 peak (~1151 cm^{-1}). We first background subtracted using the same method as for CO_2 and Neon spectra and then fit a spline to the SO_2 spectrum.

2. Statistical Significance of the MI *vs.* FI Recorded Pressures

To assess whether the pressures recorded by MI and FI are statistically different, we conducted Kolmogorov–Smirnov (KS) tests. Given the relatively small sample set sizes ($n < 50$), we performed both sample KS tests and Monte-Carlo KS tests using a Python3 routine in which we resampled 1000 times considering the uncertainties of each independent measurement. We compare the MI distributions for MI saturation pressures calculated using five different volatile solubility models (MagmaSat, Ghiorso and Gualda, 2015; MafiCH, Allison *et al.*, 2022; VolatileCalc, Newman and Lowenstern, 2002; and those of Iacono-Marziano *et al.*, 2012 and Shishkina *et al.*, 2014) with the pressure distribution from our new FI data (Fig. S-8). We note that there are very large variations in the MI saturation pressures when using different solubility models, which by themselves can largely account for the difference in the distributions (Fig. S-9). If one considers the MagmaSat solubility model, while the sample KS statistics appear significant (which would suggest that the FI are underestimating the magma storage pressures), when we consider the uncertainty on both the FI and particularly the MI measurements, the Monte-Carlo KS statistic is no longer significant for any of the three events. This suggests that the FI are predicting the same entrapment pressures as the MI, within the uncertainty of the measurements.

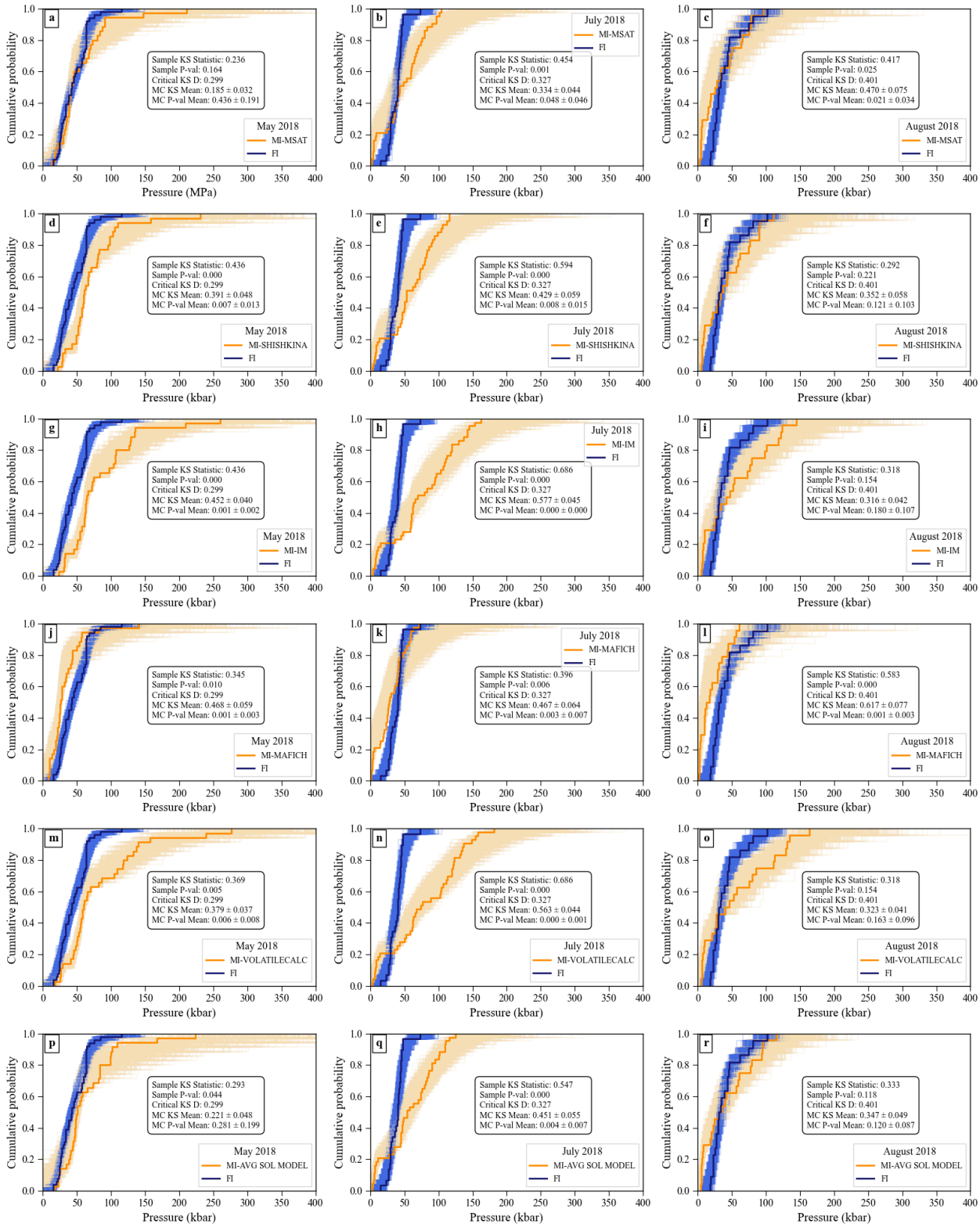

Figure S-8 Monte Carlo KS tests on cumulative distributions of pressures for FI (blue) and MI (orange) using different solubility models for each eruptive event: **(a–c)** MagmaSat ('MSAT', Ghiorso and Gualda, 2015); **(d–f)** Shishkina *et al.* (2014, 'SHISHKINA'); **(g–i)** Iacono-Marziano *et al.* (2012; 'IM'); **(j–l)** MafiCH (Allison *et al.*, 2022); **(m–o)** VolatileCalc (Newman and Lowenstern, 2002); **(p–r)** Average Solubility model (standard deviation as uncertainty).

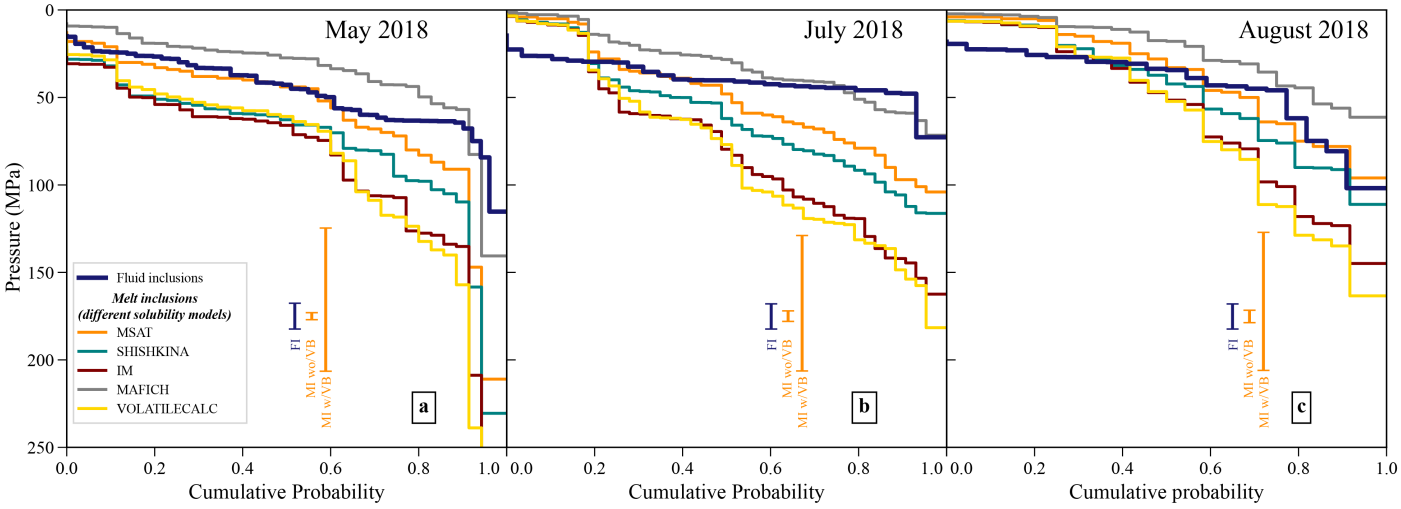

Figure S-9 Pressure CDF for comparing fluid and melt inclusion pressures for **(a)** May 2018, **(b)** July 2018 and **(c)** August 2018 using five different solubility models: MagmaSat ('MSAT'; Ghiorso and Gualda, 2015), Shishkina *et al.* (2014; 'SHISHKINA'), Iacono-Marziano *et al.* (2012; 'IM'), MafiCH (Allison *et al.*, 2022), and VolatileCalc (Newman and Lowenstern, 2002).

3. Effect of H_2O mol % in Fluid on Calculated Densities and Pressures

In relatively shallow systems like Kīlauea, the exsolved vapour phase will not be pure CO_2, but will contain some fraction of H_2O. When performing fluid inclusion studies on mixed fluids, it is generally assumed that the H_2O has been lost from the fluid inclusion. Then, the measured CO_2 density is corrected based on the molar fraction of H_2O and molar ratios (see Hansteen and Klügel, 2008). This bulk density is then entered into a mixed H_2O–CO_2 equation of state to calculate pressure.

To estimate the mol fraction of H_2O in the exsolved fluid, we examined melt inclusion data from Wieser *et al.* (2021). The solubility model MagmaSat returns the calculated pressure, and XH_2O at the point of vapour saturation. For the 2018 eruption, it is difficult to estimate the initial H_2O content at the time of melt and fluid inclusion entrapment, because H_2O was reset through diffusive re-equilibration with the carrier melt transporting crystals down the East Rift Zone. However, it has been suggested that the reservoir melts were likely drier than normal Kīlauea magmas due to mixing and degassing of summit lake lavas over the decade prior (Lerner *et al.*, 2021). To encompass this uncertainty, we show XH_2O calculated using the measured H_2O content, and 0.5 wt. % H_2O, which encompasses the higher end of the range at Kīlauea over the last few hundred years (Fig. S-10, red and blue dots, respectively). We also calculated the mean of the two (Fig. S-10b, green dots).

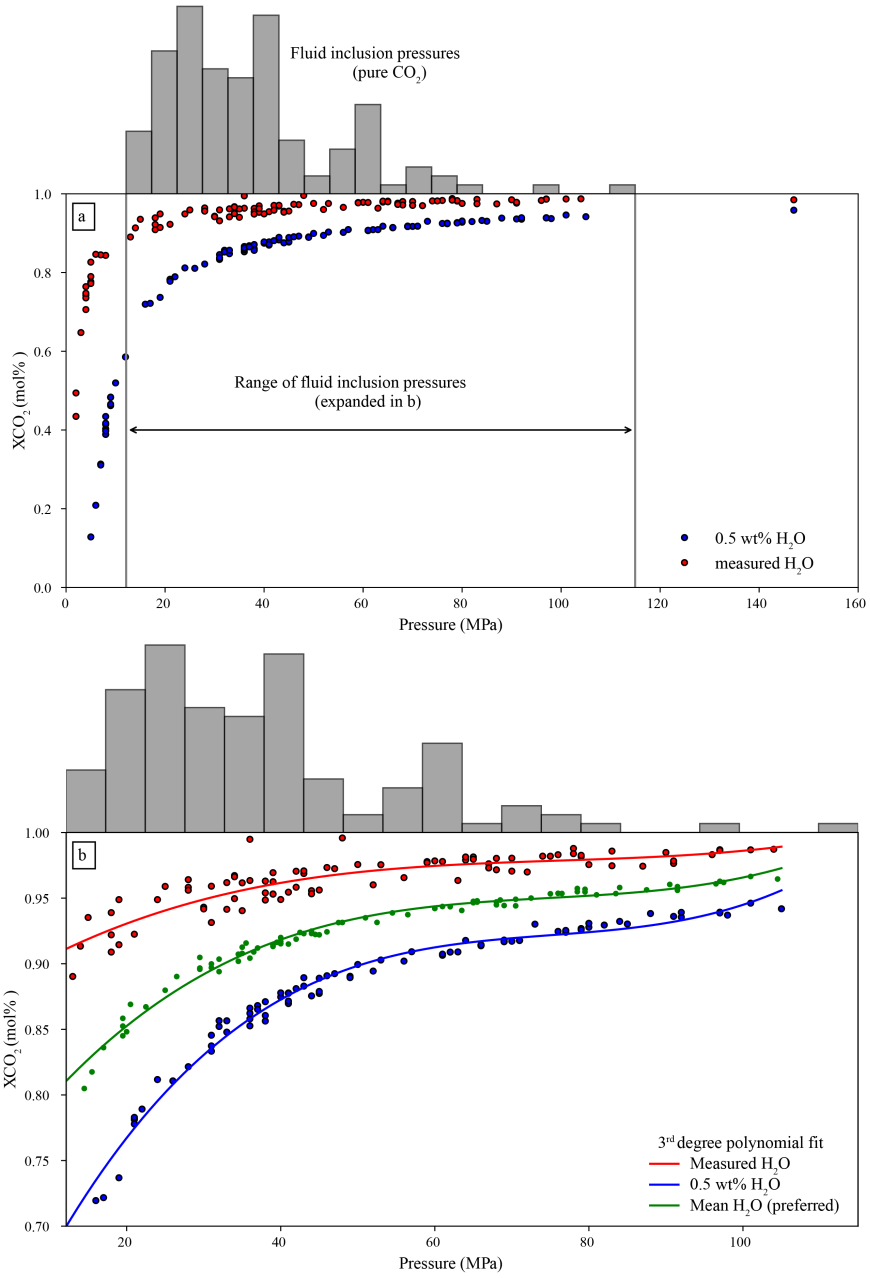

Figure S-10 $X\mathrm{CO_2}$ values from Wieser *et al.* (2021). **(a)** The entire range of measured pressures. **(b)** Enlarged view of only the pressure range observed in fluid inclusions along with 3rd degree polynomial fits. Based on inferences of $\mathrm{H_2O}$ drainback and degassing (Lerner *et al.*, 2021), we use $X\mathrm{CO_2}$ shown by the green polynomial, although we consider the uncertainty introduced by $X\mathrm{CO_2}$ between the red and blue polynomials (measured $\mathrm{H_2O}$ contents, red dots, lower plausible limit), and upper limit Kīlauea $\mathrm{H_2O}$ contents (blue dots, 0.5 wt. %, upper plausible limit).

To perform the correction, we regressed pressure *vs*. $X\mathrm{CO_2}$ (equivalent to $1 - X\mathrm{H_2O}$) using a 3rd degree polynomial (Fig. S-10b) for measured $\mathrm{H_2O}$ contents, 0.5 wt. % $\mathrm{H_2O}$ and the mean $\mathrm{H_2O}$ values. This means for each fluid inclusion we can allocate an approximate $X\mathrm{H_2O}$ value as $X\mathrm{H_2O} = 1 - X\mathrm{CO_2}$. We then calculated pressure using the mixed $\mathrm{CO_2}$–$\mathrm{H_2O}$ EOS of Duan and Zhang (2006) implemented in DiadFit v0.0.80. Given

that our initial pressures were calculated using a pure CO_2 EOS, we iterated four times to converge towards a final corrected pressure. We note that the corrected pressures and associated uncertainties are within the pure CO_2 pressures and the uncertainty estimated by the Monte Carlo simulations (Fig. S11). We used the XCO_2 value from the green (middle) scenario, but consider the uncertainty introduced by XCO_2 values between the blue and red lines.

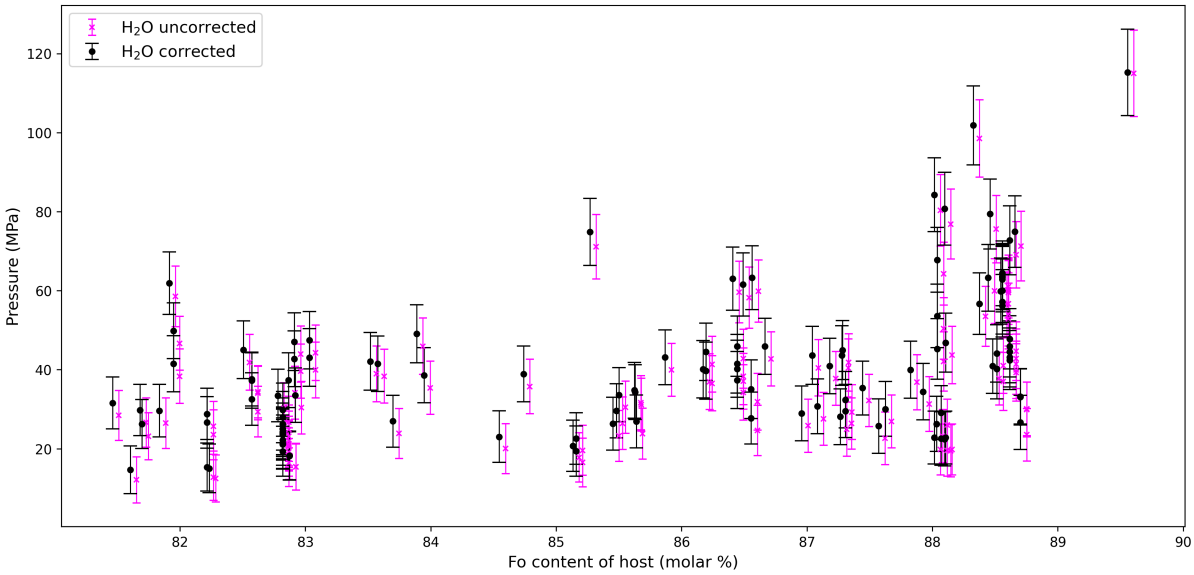

Figure S-11 Fluid inclusion pressures as a function of the Fo content of the olivine hosts. Black markers are H_2O corrected pressures, with corresponding uncertainties considering the minimum and maximum water content ranges from Figure S10 as well as the uncertainty from the Monte Carlo simulations for the pure CO_2 EOS pressures, summed in quadrature. Magenta markers show the pure CO_2 EOS pressures and are artificially offset in Fo content by 0.05 to aid visibility.

4. Fluid % Effect on Calculated Densities and Pressures

Magmatic fluid inclusions are often trapped with variable small amounts of silicate melt. We estimated the proportion of exsolved fluid to silicate melt using FIJI (Schindelin *et al.*, 2012). We filtered out of the dataset any inclusion <80 % exsolved fluid. In Figures S-12 and S-13, we plot the measured CO_2 density of FI in the same crystals, which have variable amounts of exsolved fluid. We also individually plot the FI in each crystal in subsequent panels. We found no clear trends indicating that FI with small amounts of silicate melt (<20 %) are likely to record the same conditions as those with nearly no melt at all. Some crystals show a weak relationship where FI with no melt or very little melt have record the highest densities. However, we recognise the dataset is much too small to conclude on this matter. Future work is required to constrain whether any significant relationship exists. For this study, we consider that FI with >80 % exsolved fluid offer a suitable record of pressure. This is consistent with previous work indicating that exchange of CO_2 with the melt is negligible in inclusions that trap predominantly the vapor phase (little melt) (Steele-MacInnis *et al.*, 2017).

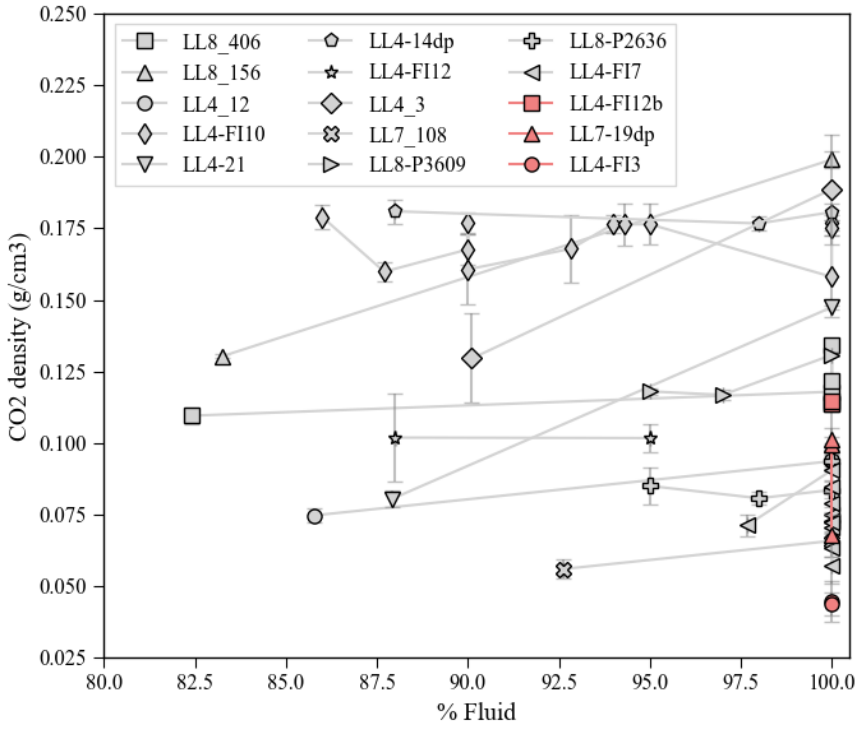

Figure S-12 Measured CO_2 density of FI against the % exsolved fluid for FI "pairs", *i.e.* FI found in the same crystals and within relative proximity to each other with apparently similar genetic relationships.

Figure S-13 Single crystal plots (pages SI-16 to SI-21). Measured CO_2 density of FI against the % exsolved fluid for FI "pairs", *i.e.* FI found in the same crystals and within relative proximity to each other with apparently similar genetic relationships.

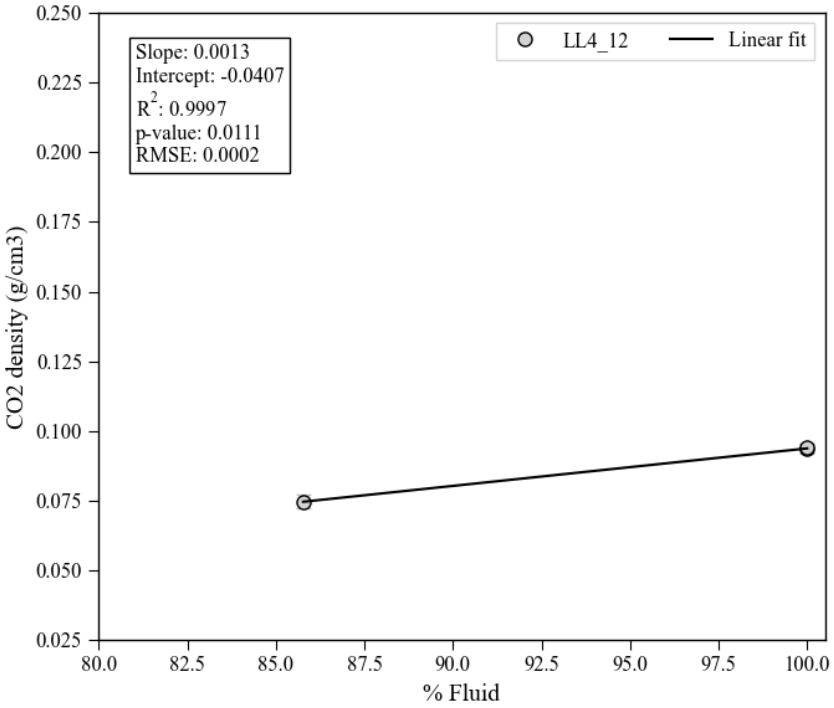
Slope: 0.0013
Intercept: -0.0407
R2: 0.9997
p-value: 0.0111
RMSE: 0.0002
LL4_12
Linear fit
CO2 density (g/cm3)
% Fluid
0.250
0.225
0.200
0.175
0.150
0.125
0.100
0.075
0.050
0.025
80.0
82.5
85.0
87.5
90.0
92.5
95.0
97.5
100.0

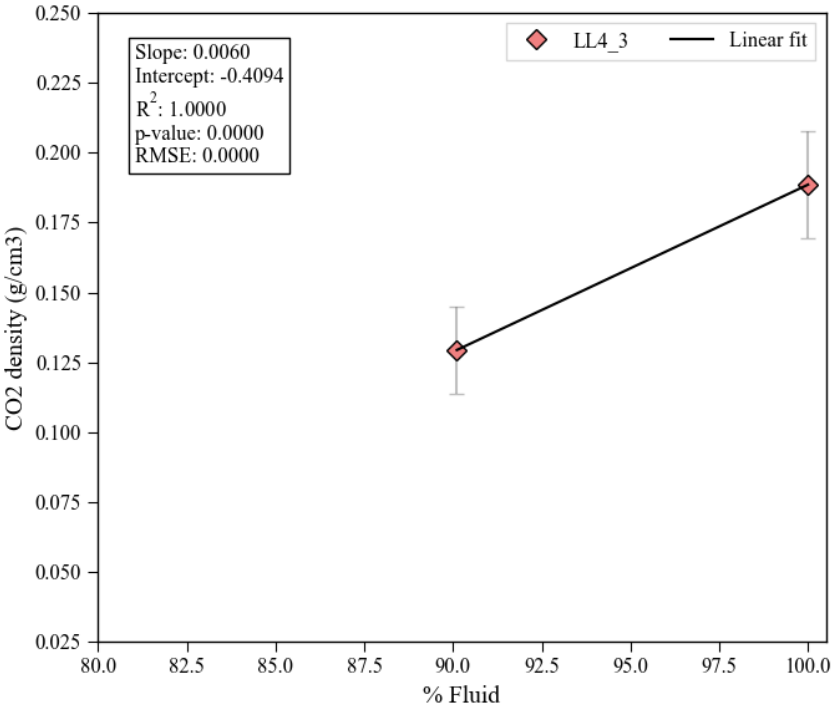
Slope: 0.0060
Intercept: -0.4094
R2: 1.0000
p-value: 0.0000
RMSE: 0.0000
LL4_3
Linear fit
CO2 density (g/cm3)
% Fluid
0.250
0.225
0.200
0.175
0.150
0.125
0.100
0.075
0.050
0.025
80.0
82.5
85.0
87.5
90.0
92.5
95.0
97.5
100.0

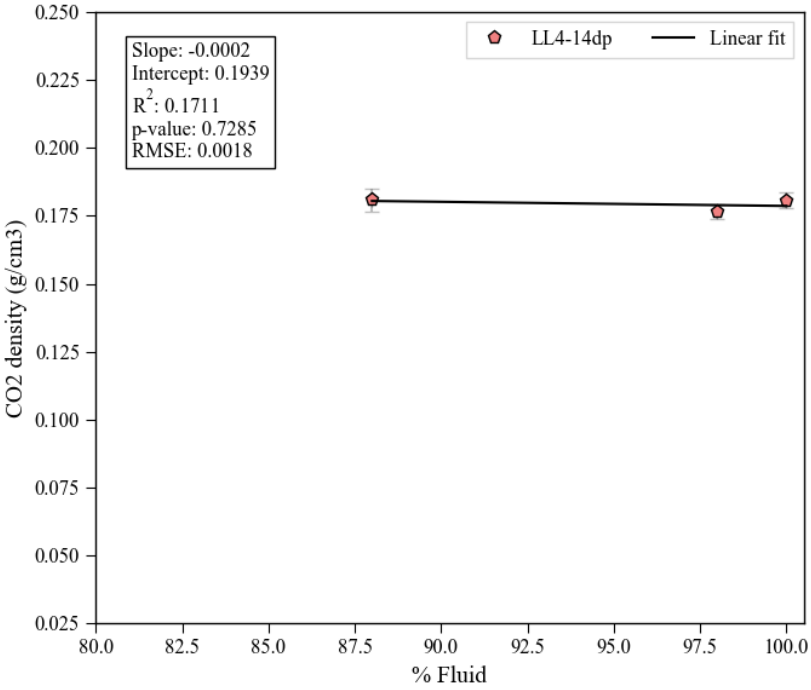
Slope: -0.0002
Intercept: 0.1939
R2: 0.1711
p-value: 0.7285
RMSE: 0.0018
LL4-14dp
Linear fit
CO2 density (g/cm3)
% Fluid
0.250
0.225
0.200
0.175
0.150
0.125
0.100
0.075
0.050
0.025
80.0
82.5
85.0
87.5
90.0
92.5
95.0
97.5
100.0

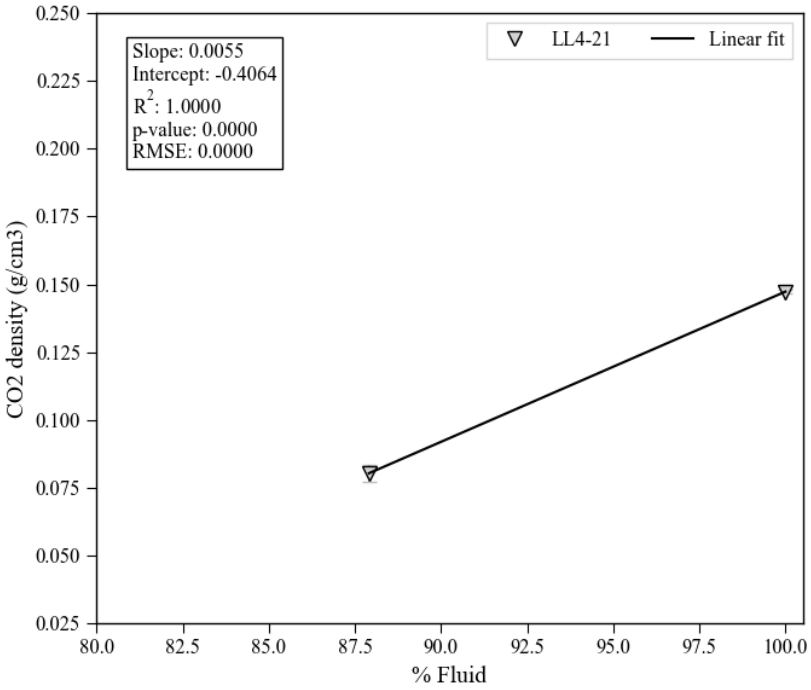
Slope: 0.0055
Intercept: -0.4064
R2: 1.0000
p-value: 0.0000
RMSE: 0.0000
LL4-21
Linear fit
CO2 density (g/cm3)
% Fluid
0.250
0.225
0.200
0.175
0.150
0.125
0.100
0.075
0.050
0.025
80.0
82.5
85.0
87.5
90.0
92.5
95.0
97.5
100.0

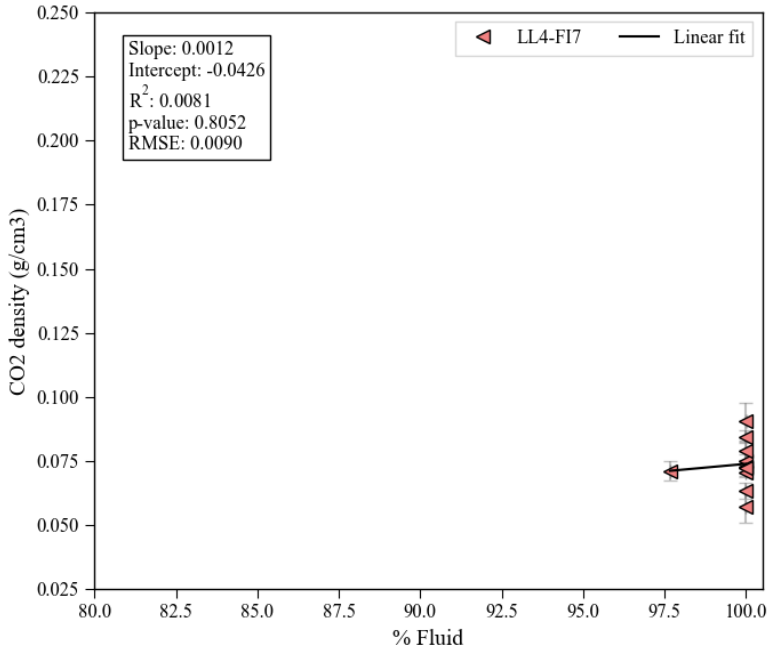
Slope: 0.0012
Intercept: -0.0426
R2: 0.0081
p-value: 0.8052
RMSE: 0.0090
LL4-FI7
Linear fit
CO2 density (g/cm3)
% Fluid
0.250
0.225
0.200
0.175
0.150
0.125
0.100
0.075
0.050
0.025
80.0
82.5
85.0
87.5
90.0
92.5
95.0
97.5
100.0

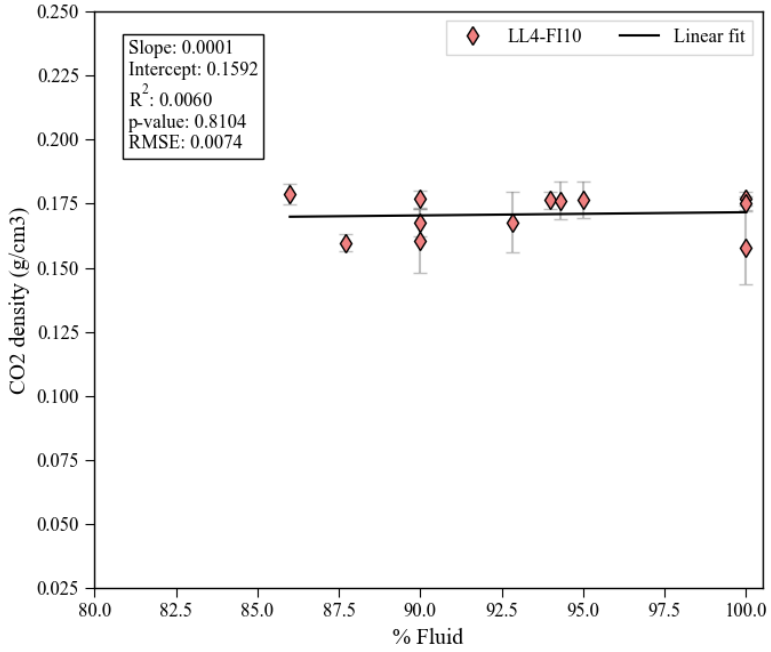
Slope: 0.0001
Intercept: 0.1592
R2: 0.0060
p-value: 0.8104
RMSE: 0.0074
LL4-FI10
Linear fit
CO2 density (g/cm3)
% Fluid
0.250
0.225
0.200
0.175
0.150
0.125
0.100
0.075
0.050
0.025
80.0
82.5
85.0
87.5
90.0
92.5
95.0
97.5
100.0

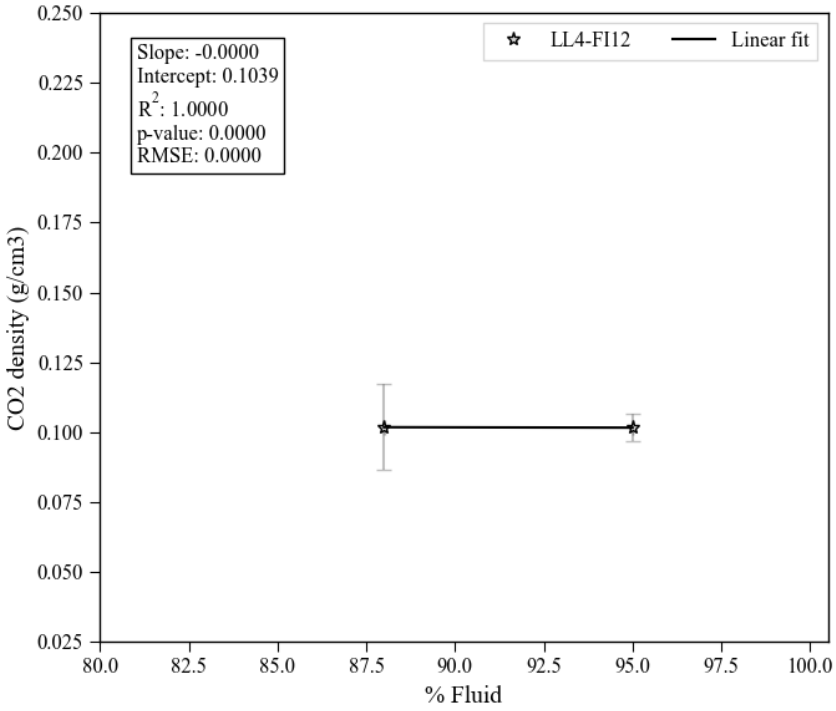
Slope: -0.0000
Intercept: 0.1039
R2: 1.0000
p-value: 0.0000
RMSE: 0.0000
LL4-FI12
Linear fit
CO2 density (g/cm3)
% Fluid
0.250
0.225
0.200
0.175
0.150
0.125
0.100
0.075
0.050
0.025
80.0
82.5
85.0
87.5
90.0
92.5
95.0
97.5
100.0

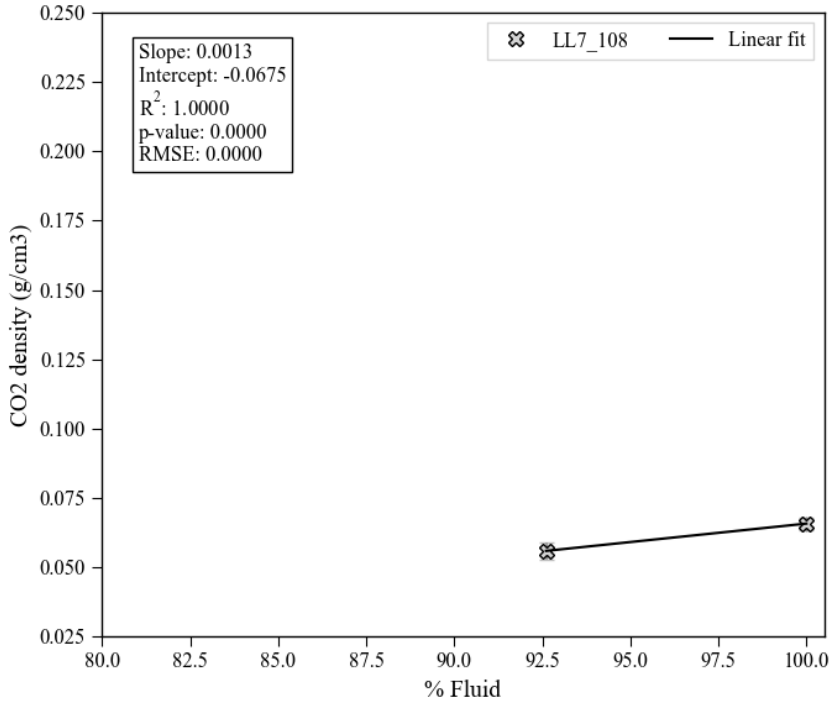
Slope: 0.0013
Intercept: -0.0675
R2: 1.0000
p-value: 0.0000
RMSE: 0.0000
LL7_108
Linear fit
CO2 density (g/cm3)
% Fluid
0.250
0.225
0.200
0.175
0.150
0.125
0.100
0.075
0.050
0.025
80.0
82.5
85.0
87.5
90.0
92.5
95.0
97.5
100.0

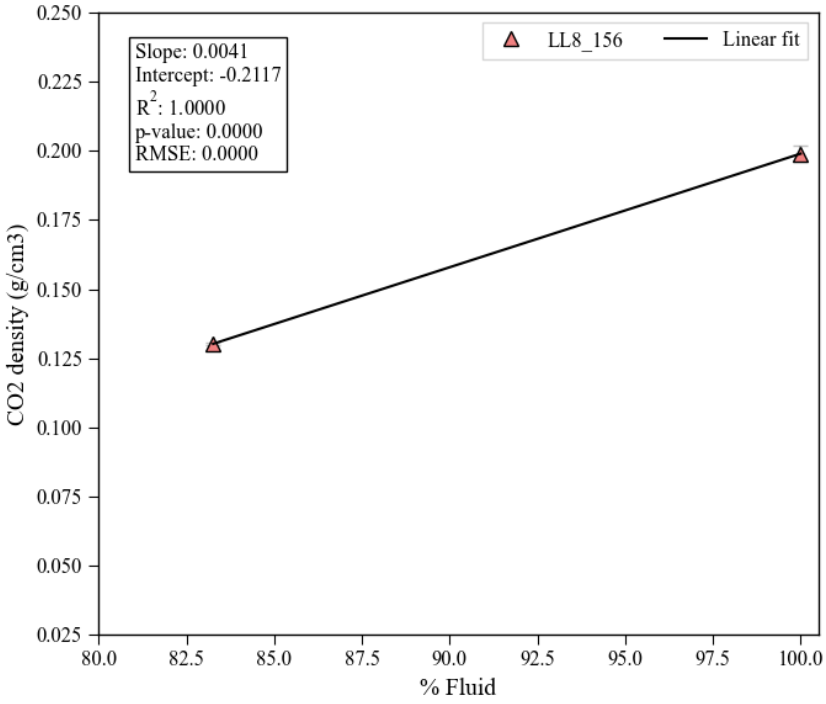
Slope: 0.0041
Intercept: -0.2117
R2: 1.0000
p-value: 0.0000
RMSE: 0.0000
LL8_156
Linear fit
CO2 density (g/cm3)
% Fluid
0.250
0.225
0.200
0.175
0.150
0.125
0.100
0.075
0.050
0.025
80.0
82.5
85.0
87.5
90.0
92.5
95.0
97.5
100.0

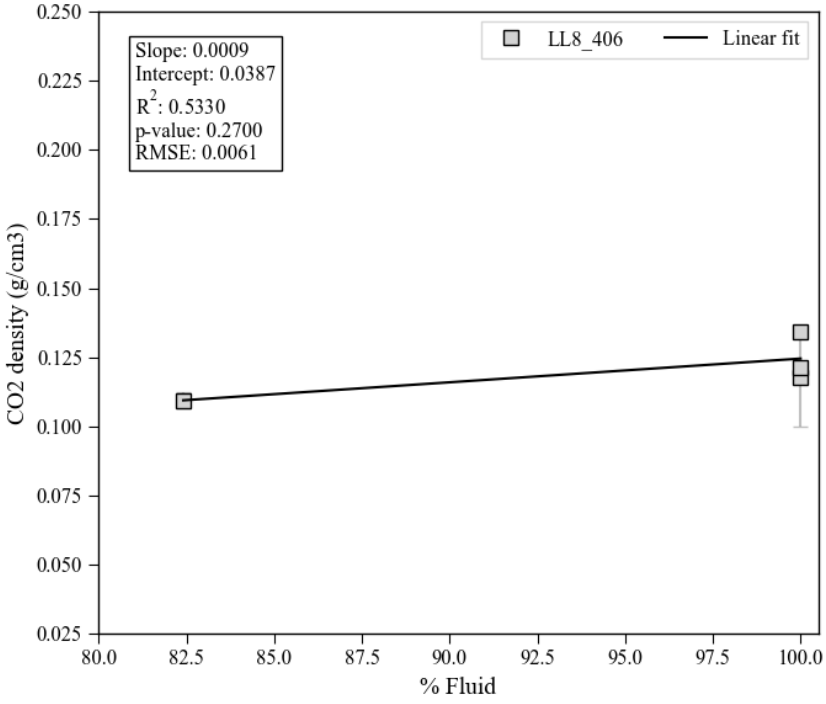
Slope: 0.0009
Intercept: 0.0387
R2: 0.5330
p-value: 0.2700
RMSE: 0.0061
LL8_406
Linear fit
CO2 density (g/cm3)
% Fluid
0.250
0.225
0.200
0.175
0.150
0.125
0.100
0.075
0.050
0.025
80.0
82.5
85.0
87.5
90.0
92.5
95.0
97.5
100.0

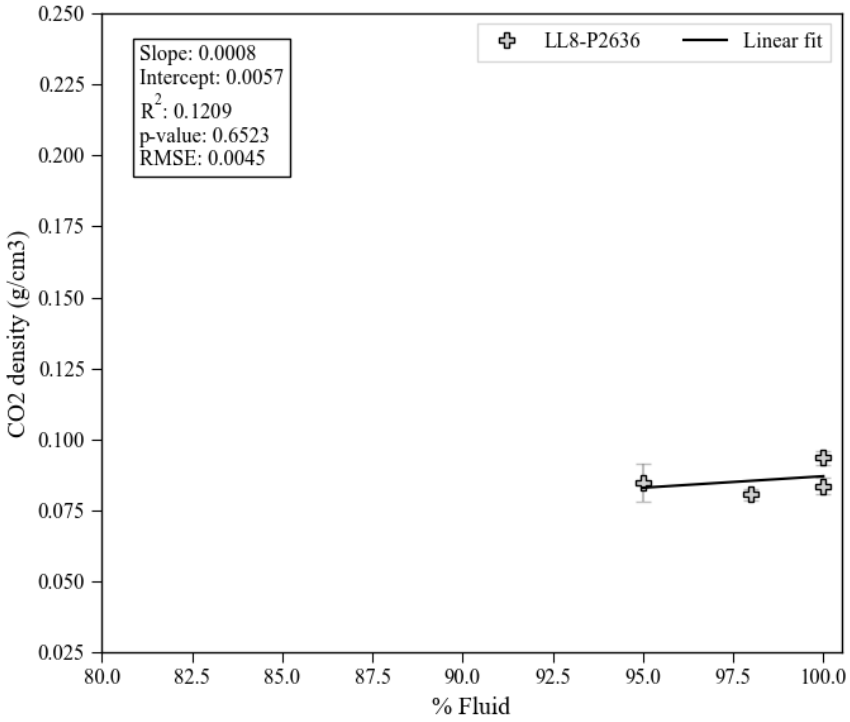
Slope: 0.0008
Intercept: 0.0057
R2: 0.1209
p-value: 0.6523
RMSE: 0.0045
LL8-P2636
Linear fit
CO2 density (g/cm3)
% Fluid
0.250
0.225
0.200
0.175
0.150
0.125
0.100
0.075
0.050
0.025
80.0
82.5
85.0
87.5
90.0
92.5
95.0
97.5
100.0

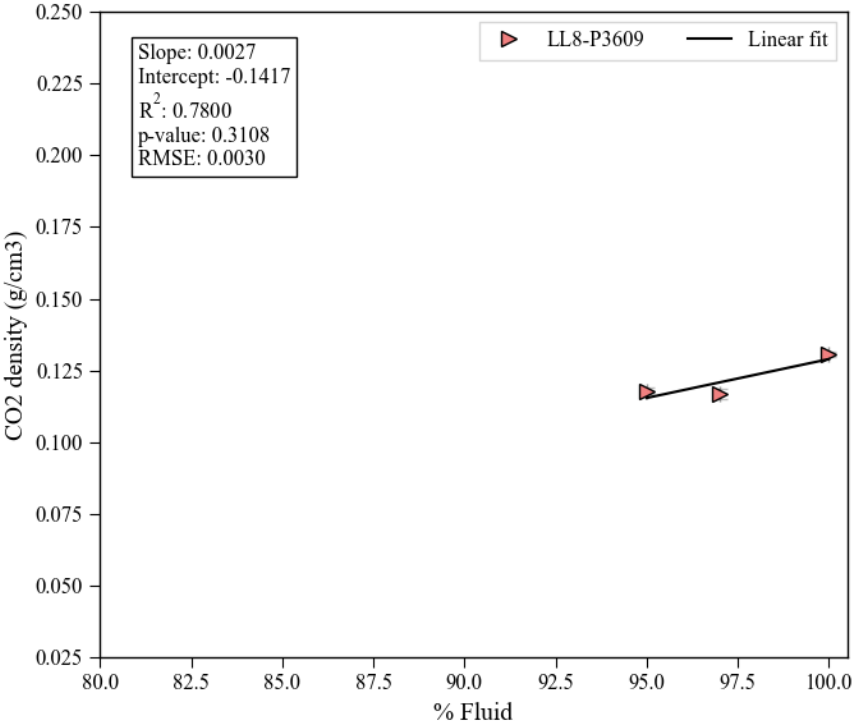
Slope: 0.0027
Intercept: -0.1417
R2: 0.7800
p-value: 0.3108
RMSE: 0.0030
LL8-P3609
Linear fit
CO2 density (g/cm3)
% Fluid
0.250
0.225
0.200
0.175
0.150
0.125
0.100
0.075
0.050
0.025
80.0
82.5
85.0
87.5
90.0
92.5
95.0
97.5
100.0

Supplementary Tables

Table S-1 Full data for each Kīlauea 2018 LERZ fluid inclusion (Raman, host olivine major element chemistry, pressure and depth calculations, and textural relationships. This is filtered for bad spectra and fluid % > 80). To see all analyses, unfiltered, unaveraged, or raw data, refer to the data repository.

Table S-2 CO_2 densities obtained *via* Raman and microthermometry for Fogo fluid inclusions. Note that in this table, repeated Raman measurements have already been averaged. For all analyses, refer to Table S-6.

Table S-3 Comparison of data fit by DiadFit v62 and DiadFit v78, for error assessment.

Table S-4 Comparison of error from peak-fitting and densimeter (output as 1sig from DiadFit) with uncertainty from repeated analyses.

Table S-5 Secondary olivine standards run for electron microprobe data; headers are the same as in Table S-1.

Table S-6 CO_2 densities obtained *via* Raman and microthermometry for all Fogo fluid inclusions. Note that in this table, repeated Raman measurements have NOT been averaged.

Table S-7 Supplementary dataset from Wieser *et al*. (2021).

Tables S-1 to S-7 are available for download (.xlsx) from the online version of this article at https://doi.org/10.7185/geochemlet.2404.

Supplementary Image Database

Supplementary images of fluid inclusions in their host crystals are available for download (.pdf) from the online version of this article at https://doi.org/10.7185/geochemlet.2404.

Supplementary Information References

Allison, C.M., Roggensack, K., Clarke, A.B. (2022) MafiCH: a general model for H_2O–CO_2 solubility in mafic magmas. *Contributions to Mineralogy and Petrology* 177, 40. https://doi.org/10.1007/s00410-022-01903-y

Blundy, J., Melekhova, E., Ziberna, L., Humphreys, M.C.S., Cerantola, V., Brooker, R.A., McCammon, C.A., Pichavant, M., Ulmer, P. (2020) Effect of redox on Fe–Mg–Mn exchange between olivine and melt and an oxybarometer for basalts. *Contributions to Mineralogy and Petrology* 175, 103. https://doi.org/10.1007/s00410-020-01736-7

Clague, D.A., Bohrson, W.A. (1991) Origin of xenoliths in the trachyte at Puu Waawaa, Hualalai Volcano, Hawaii. *Contributions to Mineralogy and Petrology* 108, 439–452. https://doi.org/10.1007/BF00303448

Clague, D.A., Moore, J.G., Dixon, J.E., Friesen, W.B. (1995) Petrology of Submarine Lavas from Kilauea's Puna Ridge, Hawaii. *Journal of Petrology* 36, 299–349. https://doi.org/10.1093/petrology/36.2.299

Dayton, K., Gazel, E., Wieser, P., Troll, V.R., Carracedo, J.C., La Madrid, H., Roman, D.C., Ward, J., Aulinas, M., Geiger, H., Deegan, F.M., Gisbert, G., Perez-Torrado, F.J. (2023) Deep magma storage during the 2021 La Palma eruption. *Science Advances* 9, eade7641. https://doi.org/10.1126/sciadv.ade7641

DeVitre, C.L., Allison, C.M., Gazel, E. (2021) A high-precision CO_2 densimeter for Raman spectroscopy using a Fluid Density Calibration Apparatus. *Chemical Geology* 584, 120522. https://doi.org/10.1016/j.chemgeo.2021.120522

DeVitre, C.L., Gazel, E., Ramalho, R.S., Venugopal, S., Steele-MacInnis, M., Hua, J., Allison, C.M., Moore, L.R., Carracedo, J.C., Monteleone, B. (2023) Oceanic intraplate explosive eruptions fed directly from the mantle. *Proceedings of the National Academy of Sciences* 120, e2302093120. https://doi.org/10.1073/pnas.2302093120

Duan, Z., Zhang, Z. (2006) Equation of state of the H_2O, CO_2, and H_2O–CO_2 systems up to 10 GPa and 2573.15 K: Molecular dynamics simulations with ab initio potential surface. *Geochimica et Cosmochimica Acta* 70, 2311–2324. https://doi.org/10.1016/j.gca.2006.02.009

Ghiorso, M.S., Gualda, G.A.R. (2015) An H_2O–CO_2 mixed fluid saturation model compatible with rhyolite-MELTS. *Contributions to Mineralogy and Petrology* 169, 53. https://doi.org/10.1007/s00410-015-1141-8

Hansteen, T.H., Klügel, A. (2008) Fluid Inclusion Thermobarometry as a Tracer for Magmatic Processes. *Reviews in Mineralogy and Geochemistry* 69, 143–177. https://doi.org/10.2138/rmg.2008.69.5

Helz, R.T., Thornber, C.R. (1987) Geothermometry of Kilauea Iki lava lake, Hawaii. *Bulletin of Volcanology* 49, 651–668. https://doi.org/10.1007/BF01080357

Helz, R.T., Clague, D.A., Sisson, T.W., Thornber, C.R. (2014) Petrologic insights into basaltic volcanism at historically active Hawaiian volcanoes. In: Poland, M.P., Takahashi, T.J., Landowski, C.M. (Eds.) *Characteristics of Hawaiian volcanoes*, USGS Professional Paper 1801. US Geological Survey, Reston, VA, 237–292. https://doi.org/10.3133/pp18016

Helz, R.T., Clague, D.A., Mastin, L.G., Rose, T.R. (2015) Evidence for Large Compositional Ranges in Coeval Melts Erupted from Kīlauea's Summit Reservoir. In: Carey, R., Cayol, V., Poland, M., Weis, D. (Eds.) *Hawaiian Volcanoes: From Source to Surface*. American Geophysical Union and Wiley, Hoboken, NJ, 125–145. https://doi.org/10.1002/9781118872079.ch7

Helz, R.T., Cottrell, E., Brounce, M.N., Kelley, K.A. (2017) Olivine-melt relationships and syneruptive redox variations in the 1959 eruption of Kīlauea Volcano as revealed by XANES. *Journal of Volcanology and Geothermal Research* 333–334, 1–14. https://doi.org/10.1016/j.jvolgeores.2016.12.006

Iacono-Marziano, G., Morizet, Y., Le Trong, E., Gaillard, F. (2012) New experimental data and semi-empirical parameterization of H_2O–CO_2 solubility in mafic melts. *Geochimica et Cosmochimica Acta* 97, 1–23. https://doi.org/10.1016/j.gca.2012.08.035

Jarosewich, E., Nelen, J.A., Norberg, J.A. (1980) Reference Samples for Electron Microprobe Analysis. *Geostandards Newsletter* 4, 43–47. https://doi.org/10.1111/j.1751-908X.1980.tb00273.x

Lamadrid, H.M., Moore, L.R., Moncada, D., Rimstidt, J.D., Burruss, R.C., Bodnar, R.J. (2017) Reassessment of the Raman CO_2 densimeter. *Chemical Geology* 450, 210–222. https://doi.org/10.1016/j.chemgeo.2016.12.034

Lerner, A.H., Wallace, P.J., Shea, T., Mourey, A.J., Kelly, P.J., Nadeau, P.A., Elias, T., Kern, C., Clor, L.E., Gansecki, C., Lee, R.L., Moore, L.R., Werner, C.A. (2021) The petrologic and degassing behavior of sulfur and other magmatic volatiles from the 2018 eruption of Kīlauea, Hawai'i: melt concentrations, magma storage depths, and magma recycling. *Bulletin of Volcanology* 83, 43. https://doi.org/10.1007/s00445-021-01459-y

Lin, F., Bodnar, R.J., Becker, S.P. (2007) Experimental determination of the Raman CH_4 symmetric stretching (v_1) band position from 1–650 bar and 0.3–22 °C: Application to fluid inclusion studies. *Geochimica et Cosmochimica Acta* 71, 3746–3756. https://doi.org/10.1016/j.gca.2007.05.016

Matzen, A.K., Baker, M.B., Beckett, J.R., Stolper, E.M. (2011) Fe–Mg Partitioning between Olivine and High-magnesian Melts and the Nature of Hawaiian Parental Liquids. *Journal of Petrology* 52, 1243–1263. https://doi.org/10.1093/petrology/egq089

Montierth, C., Johnston, A.D., Cashman, K.V. (1995) An Empirical Glass-Composition-Based Geothermometer for Mauna Loa Lavas. In: Rhodes, J.M., Lockwood, J.P. (Eds.) *Mauna Loa Revealed: Structure, Composition, History, and Hazards*, Geophysical Monograph Series 92, American Geophysical Union, Washington, D.C., 207–217. https://doi.org/10.1029/GM092p0207

Moussallam, Y., Edmonds, M., Scaillet, B., Peters, N., Gennaro, E., Sides, I., Oppenheimer, C. (2016) The impact of degassing on the oxidation state of basaltic magmas: A case study of Kīlauea volcano. *Earth and Planetary Science Letters* 450, 317–325. https://doi.org/10.1016/j.epsl.2016.06.031

Newman, S., Lowenstern, J.B. (2002) VOLATILECALC: a silicate melt–H_2O–CO2 solution model written in Visual Basic for excel. *Computers & Geosciences* 28, 597–604. https://doi.org/10.1016/S0098-3004(01)00081-4

Ryan, M.P. (1987) Elasticity and contractancy of Hawaiian olivine tholeiite and its role in the stability and structural evolution of sub-caldera magma reservoirs and rift systems. In: Decker, R.W., Wright, T.L., Stauffer, P.H. (Eds.) *Volcanism in Hawaii*, USGS Professional Paper 1350. US Geological Survey, Reston, VA, 1395–1447. https://pubs.usgs.gov/pp/1987/1350/pdf/chapters/pp1350_ch52.pdf

Schindelin, J., Arganda-Carreras, I., Frise, E., Kaynig, V., Longair, M., Pietzsch, T., Preibisch, S., Rueden, C., Saalfeld, S., Schmid, B., Tinevez, J.-Y., White, D.J., Hartenstein, V., Eliceiri, K., Tomancak, P., Cardona, A. (2012) Fiji: an open-source platform for biological-image analysis. *Nature Methods* 9, 676–682. https://doi.org/10.1038/nmeth.2019

Shea, T., Matzen, A.K., Mourey, A.J. (2022) Experimental study of Fe–Mg partitioning and zoning during rapid growth of olivine in Hawaiian tholeiites. *Contributions to Mineralogy and Petrology* 177, 114. https://doi.org/10.1007/s00410-022-01969-8

Shishkina, T.A., Botcharnikov, R.E., Holtz, F., Almeev, R.R., Jazwa, A.M., Jakubiak, A.A. (2014) Compositional and pressure effects on the solubility of H_2O and CO_2 in mafic melts. *Chemical Geology* 388, 112–129. https://doi.org/10.1016/j.chemgeo.2014.09.001

Sides, I., Edmonds, M., Maclennan, J., Houghton, B.F., Swanson, D.A., Steele-MacInnis, M.J. (2014a) Magma mixing and high fountaining during the 1959 Kīlauea Iki eruption, Hawai'i. *Earth and Planetary Science Letters* 400, 102–112. https://doi.org/10.1016/j.epsl.2014.05.024

Sides, I.R., Edmonds, M., Maclennan, J., Swanson, D.A., Houghton, B.F. (2014b) Eruption style at Kīlauea Volcano in Hawai'i linked to primary melt composition. *Nature Geoscience* 7, 464–469. https://doi.org/10.1038/ngeo2140

Span, R., Wagner, W. (1996) A New Equation of State for Carbon Dioxide Covering the Fluid Region from the Triple-Point Temperature to 1100 K at Pressures up to 800 MPa. *Journal of Physical and Chemical Reference Data* 25, 1509–1596. https://doi.org/10.1063/1.555991

Steele-MacInnis, M., Esposito, R., Moore, L.R., Hartley, M.E. (2017) Heterogeneously entrapped, vapor-rich melt inclusions record pre-eruptive magmatic volatile contents. *Contributions to Mineralogy and Petrology* 172, 18. https://doi.org/10.1007/s00410-017-1343-3

Wang, X., Chou, I.-M., Hu, W., Burruss, R.C., Sun, Q., Song, Y. (2011) Raman spectroscopic measurements of CO_2 density: Experimental calibration with high-pressure optical cell (HPOC) and fused silica capillary capsule (FSCC) with application to fluid inclusion observations. *Geochimica et Cosmochimica Acta* 75, 4080–4093. https://doi.org/10.1016/j.gca.2011.04.028

Wieser, P.E., DeVitre, C.L. (2023) DiadFit: An Open-Source Python3 Tool for Peak fitting of Raman Data from silicate melts and CO_2 fluids. *EarthArXiv*. https://doi.org/10.31223/X5CQ1F

Wieser, P.E., Edmonds, M., Maclennan, J., Jenner, F.E., Kunz, B.E. (2019) Crystal scavenging from mush piles recorded by melt inclusions. *Nature Communications* 10, 5797. https://doi.org/10.1038/s41467-019-13518-2

Wieser, P.E., Lamadrid, H., Maclennan, J., Edmonds, M., Matthews, S., Iacovino, K., Jenner, F.E., Gansecki, C., Trusdell, F., Lee, R.L., Ilyinskaya, E. (2021) Reconstructing Magma Storage Depths for the 2018 Kīlauean Eruption From Melt Inclusion CO_2 Contents: The Importance of Vapor Bubbles. *Geochemistry, Geophysics, Geosystems* 22, e2020GC009364. https://doi.org/10.1029/2020GC009364

Yuan, X., Mayanovic, R.A. (2017) An Empirical Study on Raman Peak Fitting and Its Application to Raman Quantitative Research. *Applied Spectroscopy* 71, 2325–2338. https://doi.org/10.1177/0003702817721527